INCLUSION OF PORE PRESSURE EFFECTS IN DISCRETE ELEMENT MODELING OF ROCK CUTTING

RUDY L.J. HELMONS[1], SAPE A. MIEDEMA[2] AND C. VAN RHEE[2]

[1] Delft University of Technology
Mekelweg 2, 2628 CD Delft, Netherlands
r.l.j.helmons@tudelft.nl

[2] Delft University of Technology
Mekelweg 2, 2628 CD Delft, Netherlands

Key words: Rock Cutting, DEM, SPH, poromechanics

Abstract. Many rock excavation processes occur in a marine environment, like in drilling for oil/gas, dredging, trenching and deep sea mining. The presence of a fluid in and surrounding the rock can have a significant influence on the cutting process, through differences in the ambient (confining) and pore pressure. The cutting motion deforms the rock matrix, and as a result, local fluid pressure differences will occur. The magnitude of these pressure differences, and thus its effect on the cutting process, increases with larger water depths and/or higher cutting velocities. The apparent strength of the rock matrix increases with higher confining pressures, resulting in a higher cutting force.

The Discrete Element Method is used successfully to simulate the rock cutting process of dry rock for various applications. In this paper, the authors extend DEM with a fully coupled fluid pressure model to simulate the mechanics of saturated rock. This is done by solving a pore pressure diffusion equation with a Smoothed Particle (SP) method. By using the SP, it is possible to convert the discontinuum properties of the DEM to a continuum, in which the fluid pressure is modeled and applied as an additional force in the DEM.

Qualitative results show that the model is able to capture the increase in cutting force with increasing confining pressure, as well as deformation rate effects applied on saturated rocks.

1 INTRODUCTION

An important factor in future oil and gas reserves are the costs to drill a well. These costs are influenced by the rate of penetration (ROP). The ROP becomes increasingly susceptible to the hydrostatic pressure when drilling holes at larger depths. This transition is likely to occur in the range where the hydrostatic pressure is of the same order of magnitude as the strength of the rock. Proper modeling and understanding of the phenomena

that occur when drilling rock at large depths can help in improving the performance of the drilling process.

The combination of high pressure and high deformation makes it complicated to model the cutting of rock. Several empirical and analytical models [1], [2], [3] have been developed to describe the rock cutting process. However, most of these models are specifically designed for practical purposes and are less suitable for research purposes. Knowledge about effects like the shape and size of cuttings, the amount and kind of damage to the virgin (uncut) rock, lay-out of the cutting structure on the drill bit is desired to further optimize the cutting process. The Discrete Element Method (DEM) is a powerful tool that can help to give a more detailed analysis of the rock cutting process. This has already been done for various applications: Tunneling [4], [5], dredging/alluvial mining [6], [7], [8] and (oil/gas) drilling [8], [9], [10], [11].

It is generally accepted that the drilling specific energy (amount of energy required to drill unit volume of rock), depends on the differential pressure, i.e. on the difference between the bottom-hole pressure and the virgin pore pressure. However, it has also been recognized early on that such a conceptual model is probably not applicable to low-permeability dilatant rocks because the fluid cannot be supplied rapidly enough to the failed regions, causing the pore pressure in the failed zones to drop or even vanish, as discussed by Detournay and Atkinson [2]. Results of single cutter experiments by Zijsling [12] support this view.

The existing DEM models for drilling are thus far based on application of the differential pressure, automatically assuming dry rock [9], [10], [11]. Therefore, these models lack the influence of a changing pore pressure. In this paper, an approach that considers the dynamically changing pore pressures is presented. This paper is a further improvement of the work presented in [6].

2   PRESSURE EFFECTS

The influence of the fluid pressure on the cutting process can be estimated through the pore Peclet number, which can be interpreted as the ratio of deformation rate over the pore pressure dissipation rate. According to Detournay and Atkinson [2], the pore Peclet number ζ_{Pe} is given by

$$\zeta_{Pe} = \frac{v_c t_c}{4D} = \frac{v_c t_c n \mu C_f}{4\kappa} \tag{1}$$

with cutting velocity v_c, cutting thickness t_c, pore pressure diffusivity coefficient D, dynamics fluid viscosity μ, porosity n, fluid compressibility C_f and intrinsic permeability κ in m^2. In general, it can be assumed that when $\zeta_{Pe} < 1$, the dynamic pore pressure changes are negligible and that the process can be considered as drained. In case $\zeta_{Pe} > 1$, the effect of the pore pressure changes can significantly influence the cutting process, this regime is often referred to as the undrained regime. The most profound phenomena that are observed in uni-axial and tri-axial tests with varying axial strain rates are:

1. Dilative strengthening [13], [14].

2. Compactive weakening [14].

3. Cavitation (complete loss of pore pressure, as observed in Mancos shale [12]).

3   METHOD

3.1   Discrete element method - Rock

In DEM, the solid material is represented as a collection of particles (these can be any arbitrarily shape, most often spheres in 3D or discs with unit thickness in 2D are used for the sake of simplicity) that have mutual interactions in normal and tangential directions. This paper gives the description and results in 2D. The translational and rotational motion of a particle is governed by the standard equations of rigid body mechanics

$$m_i \vec{a}_i = \vec{F}_i \tag{2}$$
$$I_i \vec{\alpha}_i = \vec{T}_i \tag{3}$$

$\vec{F}$ and $\vec{T}$ are the sums of all forces and moments applied to the particle i due to external loading, contact interactions with neighboring objects and from damping in the system. The interaction force between a pair of particles can either consist of a collision type or a bond type of interaction. In both cases the force is decomposed into normal and tangential components, with

$$\vec{F} = \vec{F}_n + \vec{F}_t = \vec{n} F_n + \vec{t} F_t \tag{4}$$

where $\vec{n}$ is the unit vector normal to the particle surface at the point of interaction. The contact forces F_n and F_t are determined with a constitutive model for the interaction. At the beginning of each simulation, a bond is installed between neighboring particles. These bonds are defined by a linear elastic perfect brittle model (see figure 1), meaning that a bond breaks immediately when its strength is exceeded. Note that a bond can break either in normal (tension) or in tangential (shear) direction and not in compressive direction (macroscopic compressive failure is considered as a localization of many micro-shear and tensile failures). After a bond is broken, the bond will be removed from the simulation. Broken bonds and new interactions are considered as collisions between two particles. For stability, numerical damping as in [15] has been applied.

The DEM can be regarded as a micro-mechanical model, with the contact and bond model parameters being micro-parameters. It is assumed that with the adequate micro-mechanical parameters macroscopic rock properties are obtained, of which the Young's modulus E, Poisson ratio ν, and compressive and tensile strengths σ_c and σ_t are the most relevant. These properties will be used in calibrating the micro-mechanical model to sufficiently mimic the macroscopic rock mechanics.
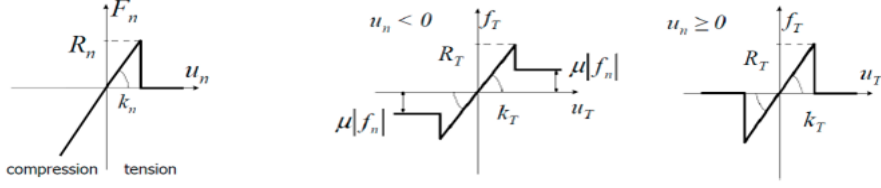
Figure 1: Linear elastic perfect brittle bond model: (left) normal direction, (middle) shear direction with contact after failure and (right) shear direction without contact after failure

3.2 Smoothed particle approach - fluid pressure

The effect of a rapidly changing effective stress is modeled with the use of a pore pressure diffusion equation, as in [16]. This equation is based on the combination of mass conservation, Darcy flow and a constitutive equation for the compressibility of the pore fluid, given respectively by

$$\frac{D\zeta}{Dt} + \nabla \cdot \vec{u} = 0 \tag{5}$$

$$\vec{u} = -\frac{\kappa}{\mu}\nabla p \tag{6}$$

$$p = M\left(\zeta - \alpha\epsilon_v\right) \tag{7}$$

which through substitution results in the pore pressure diffusion equation given by

$$\frac{Dp}{Dt} - M\nabla \cdot \left(\frac{\kappa}{\mu}\nabla p\right) = -\alpha M \frac{D\epsilon_v}{Dt} \tag{8}$$

with pressure p, fluid bulk modulus M, intrinsic permeability κ, dynamic fluid viscosity μ, effective stress coefficient α and volumetric strain ϵ_v. The coupling of the discrete data obtained from the DEM computations with the pore pressure diffusion equation (3.2) is obtained by using a Smoothed Particle (SP) approach. DEM and SP work in a co-located fashion, meaning that both methods use the same discretisation points.

In the DEM-SP model, the discretized particles are taken from a particle size distribution and randomly stacked together. The unstructured positions and random size (and thus mass) of the particles can easily result in numerical instabilities and inaccuracies. To adjust for the random size and positioning of the particles, the Corrective Smoothed Particle Approach (CSPM) is used ([17]).

In CSPM, the kernel interpolation of a field quantity A (which can be any arbitrary parameter) is calculated by

$$A\left(\vec{r}_i\right) = \frac{\sum_j A_j m_j W\left(\vec{r}_i - \vec{r}_j, h\right)}{\sum_j m_j W\left(\vec{r}_i - \vec{r}_j, h\right)} \tag{9}$$

with particle mass m, kernel function W, position r, smoothing length h, index $_i$ for particle under consideration and index $_j$ for neighboring particles (including particle $_i$).

In a similar fashion, the first order derivative of a function A is determined by

$$\nabla_i A\left(\vec{r}_i\right) = \frac{\sum_j \left(A_i - A_j\right) m_j \nabla W\left(\vec{r}_i - \vec{r}_j, h\right)}{\sum_j \left(\vec{r}_i - \vec{r}_j\right) m_j \nabla W\left(\vec{r}_i - \vec{r}_j, h\right)} \tag{10}$$

where ∇_i is the gradient with respect to particle $_i$. Higher order derivatives cannot be calculated directly. The first derivative is necessary to determine the volumetric strain rate in equation (3.2),

$$\dot{\epsilon}_v = \nabla \cdot \vec{v} = \frac{\partial v_x}{\partial x} + \frac{\partial v_y}{\partial y} \tag{11}$$

Here the Wendland C2 kernel function is used [18]

$$W = \begin{cases} \frac{7}{\pi^2}\left(1 - R\right)^4\left(4R + 1\right) & \text{if} \quad R \leq 1 \\ 0 & \text{if} \quad R > 1 \end{cases} \tag{12}$$

where

$$R = \frac{||\vec{r}_i - \vec{r}_j||}{h} \tag{13}$$

To calculate the diffusive term in (3.2), we make use of the results of [19]:

$$\nabla \cdot \kappa \nabla p = \sum_j \frac{m_j\left(\kappa_i + \kappa_j\right)}{\rho_i}\left(p_i - p_j\right)\frac{\vec{n}_{ij} \cdot \nabla W\left(\vec{r}_i - \vec{r}_j, h\right)}{||\vec{r}_i - \vec{r}_j||} \tag{14}$$

where $\vec{n}_{ij}$ is the normal unit vector of the neighboring particle centers. Note that here κ is a property of the particles and thus that it can differ throughout the rock sample. In our case, it is assumed that κ is constant.

Two way coupling is applied every timestep. DEM is advanced half a timestep, based on the intermediate velocities the volumetric strain rate is calculated with SP. This is then used to advance the pore pressure diffusion one timestep in a forward Euler scheme. The local pressure gradient of the fluid is calculated based on the new pore pressure distribution. The pressure gradient is then added as an interaction force to the sum of forces acting on the particles through

$$\vec{F} = -\nabla p \frac{\pi d_p^2}{4} w \tag{15}$$

with particle diameter d_p and unit thickness w. Finally the DEM is advanced the second half timestep.

It is possible that the fluid pressure drops below the vapor pressure during simulations. When this happens, the liquid will vaporize and as a result, the compressibility of the fluid of increases with several orders of magnitude. In the simulations, this is modeled through a simplified approach. When the pressure drops below the pressure minimum, the pressure value is fixed at the minimum pressure. From thereon it is only possible to increase the pressure by having fluid flow towards the cavitated zone, so if

$$p_i < p_{min} \quad \text{then} \quad p_i = p_{min} \quad \text{and} \quad \frac{\partial p_i}{\partial t} = \max\left(\frac{\partial p_i}{\partial t}, 0\right) \tag{16}$$

3.3 Boundary conditions

In DEM-SP, boundary conditions have to be applied for both the rock and fluid phase. For rock this is done by restricting or prescribing the motion of specific particles or walls. In case of the fluid pressure, the boundary conditions are somewhat harder to set. The SP discretisation of (3.2) in itself automatically applies Neumann boundary condition (zero gradient), meaning that it allows no fluid flow across the boundaries of the rock. This is applicable in the case where equipment is moving through the rock (cutting teeth, compressive tests, splitting tests, etc.). In case of a rock boundary that is in contact with clear fluid, like the top layer of the seabed, a Dirichlet boundary condition (fixed value, such as hydrostatic pressure) is applied. However, the boundaries of the rock may change during the simulation. Therefore it is necessary to use a method to determine what particles are part of the rock boundary. To determine this, we make use of the divergence of position, as suggested by [20].

$$\nabla \cdot \vec{r} = \frac{\partial x}{\partial x} + \frac{\partial y}{\partial y} = 2 \tag{17}$$

This is applied to the standard Smoothed Particle approach of [21], because otherwise the CSPM in equation (3.2) automatically corrects for the particle deficiency, always setting at a value of 2.

$$\nabla_i A \left(\vec{r_i} \right) = \sum_j m_j \frac{A_j}{\rho_j} \nabla W \left(\vec{r_i} - \vec{r_j}, h \right) \tag{18}$$

In the interior domain of the rock, equation (3.3) is valid. However, at the boundaries this value differs due to particle deficiency, see figure 2. Here, particles with $\nabla \cdot \vec{r} \leq 1.5$ are considered to be part of the boundary. With this technique, the particles that require a Dirichlet boundary condition can now be identified.
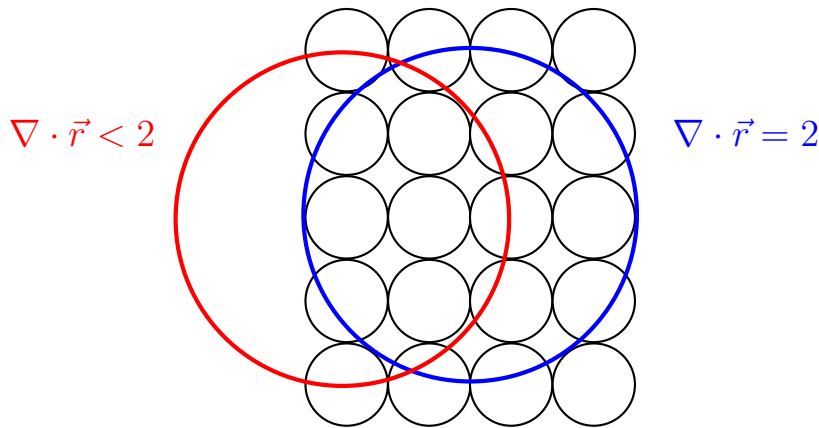
Figure 2: Schematic overview of particle deficiency

4 RESULTS

We compare the results of our approach with the experiments of Kaitkay and Lei [22]. They performed rock cutting experiments on Carthage marble. The model is calibrated to match the Youngs' modulus and the compressive strength of the rock. The used material properties are shown in table 1. A uniform particle size distribution with sizes ranging from 0.125 to 0.163 mm is used. In our approach, we used point contact bonds.

Table 1: Properties of Carthage marble and simulation specimen

Property	Carthage marble [22]	DEM-SP
E [GPa]	44.8	41.9
ν [-]	0.24	0.22
σ_c [MPa]	103	97
σ_c at $p_c = 34.5$ [MPa]	186	160
σ_{BTS} [MPa]	not published	6.3

The model for the cutting experiments is 50 mm in length and 16 mm in height. The bottom and sides of the specimen are constrained with walls to represent the surrounding rocks. The top layer is exposed to a hydrostatic pressure and flow of pore fluid through the top layer to the surrounding (clear) fluid is allowed.

Cutting simulations were performed for three pressure states (0.1, 3.5 and 34.5 MPa) and two rake angles ($\alpha = -15$ and $\alpha = -25$ deg) with cutting speed and depth of cut kept at 1 m/s and 0.8 mm, respectively.

The averaged cutting forces of our approach are compared with the experimental data of [22] in figure 3. The calculated cutting forces in our simulations are scaled with the length of the perimeter of the cutter that is in contact with the virgin rock, which is estimated as 11.3 mm for the experiments of [22].

In figure 5, it is shown what the influence of the pore Peclet number (here scaled by adjusting the pore pressure diffusion coefficient) on the cutting forces will be. An impression of the amount of damage that occurs during cutting is shown in figures 6 and 7. Note that damage here is defined as $D = \frac{\text{nr of broken bonds}}{\text{total initial bonds}}$. Lastly, snapshots of the pressure distribution during the same cutting experiments are shown in figures 8 and 9.

suggest: is apparent from a comparison of figure 3 and 4.

5 DISCUSSION

The trend of the simulated cutting force matches well with the cutting forces measured in the experiments is apparent from a comparison of figures 3 and 4. However, it must be noted that the horizontal forces show much better resemblance than the vertical components.
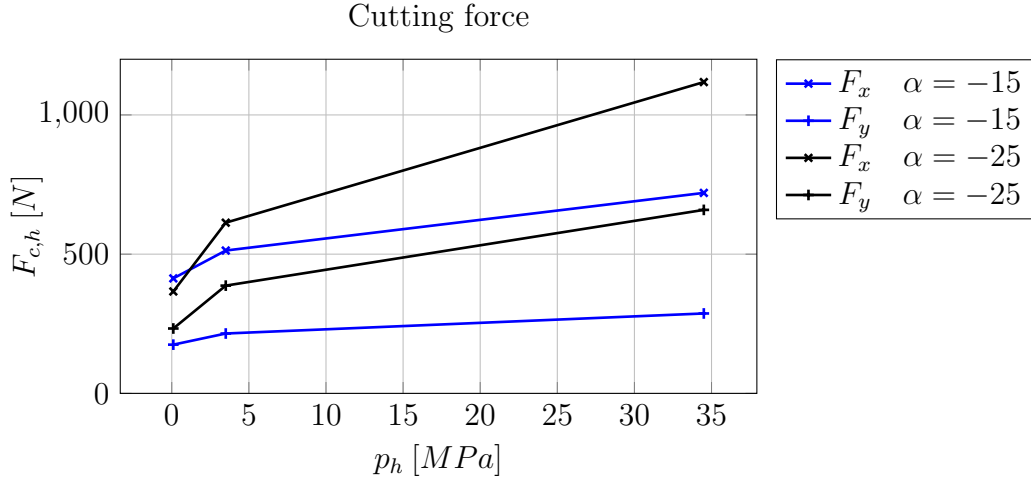
Cutting force

**Figure 3**: Cutting force vs hydrostatic pressure, simulations with DEM-SP.
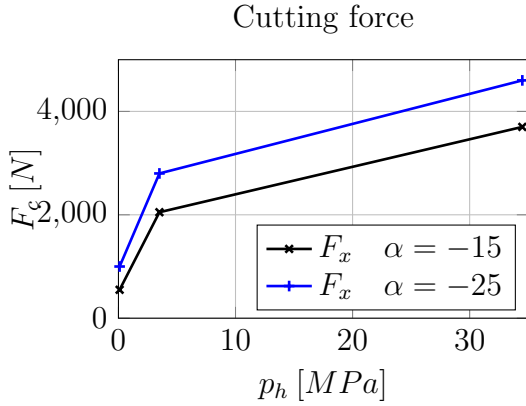
Cutting force

Figure 4: Cutting force vs hydrostatic pressure, experiments [22].

Cutting force at 34.5 MPa
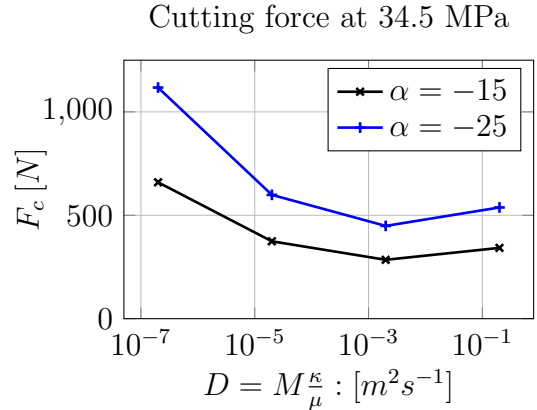
Figure 5: Cutting force vs pore pressure diffusivity.

In both the experiments and in our approach, a distinction can be noticed between brittle cutting at low hydrostatic pressures and ductile cutting at high hydrostatic pressures. This transition is also noticable when comparing the amount of damage that occurs to the DEM particles during cutting. The amount of damage and the number of fully damaged particles is significantly higher at high hydrostatic pressures, which can be observed by comparing figures 6 and 7. It also seems that after the material has been cut, some sort of filter cake is being left. The shape of the filter cake is rather smooth, which seems more realistic compared to the 'velcro'-like structures that are obtained by the method of Lei and Kaitkay [9]. Also the size of the filter cake seems to increase with increasing
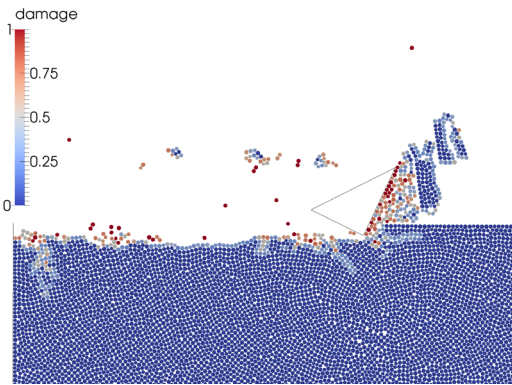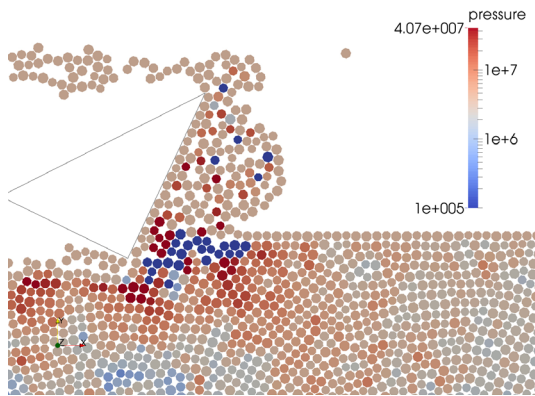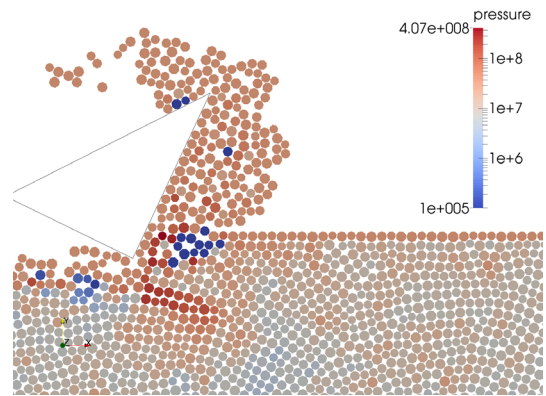
Figure 6: Damage during cutting with bit at $\alpha = -25$ and at $p_h = 0.1$ MPa.
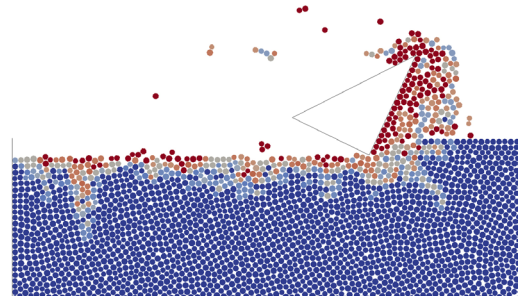
Figure 7: Damage during cutting with bit at $\alpha = -25$ and at $p_h = 34.5$ MPa.

Figure 8: Snapshot of pressure distribution during cutting with bit at $\alpha = -25$ and at $p_h = 3.5$ MPa.

Figure 9: Snapshot of pressure distribution during cutting with bit at $\alpha = -25$ and at $p_h = 34.5$ MPa.

confining pressures.

The occurrence of cavitation is clearly shown in figures 8 ($p_h = 3.5$ MPa) and 9 ($p_h = 34.5$ MPa). These figures show typical snapshots of the cutting process. The cavitating zone is located along the shear failure that occurs between the tip of the drill bit and the surface of the intact rock. Due to dilation of the particles along the shear failure, locally the pore pressure drops. The pressure drop is that large that the fluid will cavitate, which limits the local pressure gradient and effectively also limiting the required cutting force. It should be noted that the cavitating zone is larger at lower hydrostatic pressure.

In figure 5, results are shown where the pore pressure diffusion coefficient $D = M\frac{\kappa}{\mu}$ has been varied. In practice, this can be represented by varying the permeability of the rock (for instance, compare two rocks that have same strength and stiffness, but different

permeability). This is one approach to vary the pore Peclet number. It is also possible to alter the pore Peclet number by changing the pore volume deformation rate in the rock (i.e. many small pores or few bulk pores). An obvious way of changing the pore Peclet number this way is by changing the process parameters: cutting speed and cutting depth (effects for the difference between e.g. rotary drilling and mud motor drilling). A minimum in the cutting force with respect to the pore pressure diffusion coefficient can be observed. This is most likely due to the mutual interaction of compaction weakening and dilatant strengthening, of which both might dominant in a different regime of the pore Peclet number, i.e. dilatant strengthening is especially dominant in the undrained regime, while compaction weakening is more typical for slower processes, as is shown in [14].

Quantitatively, the values calculated by DEM-SP underestimate the measured values. The most profound reasons why the results underestimate the experiments are likely:

- The tensile strength in the simulation might deviate significantly from that of the experiments. However, the tensile strength in the experiments is not known. Based on [23] it is expected that the BTS value in the experiments would be approximately 10 MPa in this case of marble.

- Friction of the particles along the drill bit is underestimated. The disc-shaped particles tend to roll too easily compared to real grains.

- In 2D-DEM it is automatically assumed that the process is plane strain, while in practice the cutting process is 3D. The same effect was noted by [4].

- A different particle size distribution might improve the results. Now a small distribution is used, but a wider PSD might give a less structured rock and a less structured damage pattern.

- A cutting thickness of three particles is quite low, especially for the fluid pressure calculation (three particles thickness is getting close to the minimum number of neighbors that are required for numerical stability).

- By using parallel bonds instead of contact bonds it might be possible to increase the post-failure strength of the rock.

- The poro-mechanical properties of the numerical rock may differ significantly with those of the real rock (e.g. compactant vs. dilative, porosity).

6 CONCLUSION

By using the combination of DEM and SP to simulated the deformation of saturated rock can help in research for cutting processes. The smoothed particle approach is shown to be useful to interpolate discrete information of individual DEM particles to a continuum

field, and again the SP can be used to relate continuum properties (e.g. pore pressure, heat conduction) to the individual DEM particles. Although the results that we have obtained match qualitatively with experiments, quantitative results require further improvement.

7 ACKNOWLEDGMENTS

REFERENCES

[1] Nishimatsu, Y. The mechanics of rock cutting. *International Journal of Rock Mechanics and Mining Sciences* (1972) **9**:261-270.

[2] Detournay, E. and Atkinson, C. Influence of pore pressure on the drilling response in low-permeability shear-dilatant rocks. *International Journal of Rock Mechanics and Mining Sciences* (2000) **37-7**:1091-1101

[3] Miedema, S.A. and Zijsling, D. Hyperbaric rock cutting. In *OMAE2012*, Rio de Janeiro, Brasil, (2012).

[4] Rojek, J. and Labra, C. and Su, O. and Onate, E. Discrete element simulation of rock cutting. *Internatinal Journal of Rock Mechanics and Mining Sciences* (2011) **48-6**: 996-1010.

[5] Moon, T. and Oh, J. A study of optimal rock-cutting condition for hard rock TBM using the discrete element method. *Rock Mechanics and Rock Engineering* (2011) **45**: 837-849.

[6] Helmons, R.L.J. and Miedema, S.A. and van Rhee, C. A New Approach to Model Hyperbaric Rock Cutting Processes. In *OMAE2014*, San Francisco, California, USA, (2014).

[7] Rojek, J. Discrete element thermomechanical modeling ofrock cutting with valuation of tool wear. *Computational Particle Mechanics* (2014) **1-1**:71-84.

[8] Huang, H. and Lecampion, B. and Detournay, E. Discrete element modeling of tool-rock interaction I: rock cutting. *International Journal for Numerical and Analytical Methods in Geomechanics* (2013) **37-13**: 1913-1929.

[9] Lei, S. and Kaitkay, P. Distinct element modeling of rock cutting under hydrostatic pressure. *Key Engineering Materials* (2003) **250**: 110-117.

[10] Ledgerwood, R. PFC modeling of rock cutting under high pressure conditions. In *Rock Mechanics: Meeting Societys Challenges and Demands, Proceedings of the 1st Canada-US Rock Mechanics Symposium*, Vancouver, Canada. (2007)

[11] Mendoza Rizo, J. *Considerations for discrete element modeling of rock cutting* Diss. University of Pittsburgh, (2013).

[12] Zijsling, D.H. Single cutter testing-a key for PDC bit development. *Society of Petroleum Engineers*, Richardson, TX, 1987.

[13] Brace, W. and Martin, R. A test of the law of effective stress for crystalline rocks of low porosity *International Journal of Rock Mechanics and Mining Sciences* (1968) **5**: 415-426.

[14] Swan, G. and Cook, J. and Bruce, S. and Meehan, R. Strain rate effects in Kimmeridge bay shale *Int. J. Rock Mech. Min. Sci.* (1989) **26-2**: 135-149.

[15] Potyondy, D.O. and Cundall, P.A.A. A bonded-particle model for rock, *International journal of rock mechanics and mining sciences*, (2004), **41-8**: 1329-1364.

[16] Coussy, P.O. *Poromechanics* John Wiley and Sons Ltd., (2004).

[17] Chen, J.K. and Beraun, J.E. and Carney, T.C. A corrective smoothed particle method for boundary value problems in heat conduction. *International Journal for Numerical Methods in Engineering* (1999) **148-1**: 227-264.

[18] Wendland, H. Piecewise polynomial, positive definite and compactly supported radial functinos of minimal degree. *Advances in Computational Mathematics* (1995) **4**: 389-396.

[19] Cleary, P.W. and Monaghan, J.J. Conduction modelling using Smoothed Particle Hydrodynamics. *Journal of Computational Physics* (1999) **148-1**: 227-264.

[20] Muhammad, N. and Rogers, B.D. and Li, L. Understanding the behaviour of pulsed laser dry and wet micromachining processes by multi-phase smoothed particle hydrodynamics (SPH) modelling. *Journal of Physics D: Applied Physics* (2013) **46-9**: 095101.

[21] Lucy, L. A numerical approach to the testing of the fission hypothesis *Astronomical Journal* (1977): 1013-1024.

[22] Kaitkay, P. and Lei, S. Experimental study of rock cutting under external hydrostatic pressure. *Journal of Materials Processing Technology* (2005) **159-2**: 206-213.

[23] Hoek, E. and Kaiser, P.K. and Bawden, W.F., *Support of underground excavations in hard rock*. Balkema Rotterdam.(1995)